

Research Article

Effect of Carbon Modification on the Electrical, Structural, and Optical Properties of TiO₂ Electrodes and Their Performance in Labscale Dye-Sensitized Solar Cells

R. Taziwa,¹ E. L. Meyer,¹ E. Sideras-Haddad,² R. M. Erasmus,²
E. Manikandan,³ and B. W. Mwakikunga^{4,5}

¹Institute of Technology, University of Fort Hare, Private Bag X1314, Alice 5700, South Africa

²Center of Excellence in Strong Materials, School of Physics, University of Witwatersrand, Braamfontein 2000, Johannesburg, South Africa

³Nano Research Centre, PNTC, B. S. Abdur Rahman University, Chennai 600048, India

⁴CSIR National Centre for Nano-Structured Materials, P. O. Box 395, Pretoria 001, South Africa

⁵Department of Physics, University of Malawi-The Polytechnic, Private Bag 303, Chichiri, Blantyre 3, Malawi, South Africa

Correspondence should be addressed to B. W. Mwakikunga, bmwakikunga@csir.co.za

Received 6 February 2012; Accepted 15 June 2012

Academic Editor: Latika Menon

Copyright © 2012 R. Taziwa et al. This is an open access article distributed under the Creative Commons Attribution License, which permits unrestricted use, distribution, and reproduction in any medium, provided the original work is properly cited.

Carbon-modified titanium dioxide nanoparticles (C:TiO₂ NPs) have been synthesized by ultrasonic nebulizer spray pyrolysis (USP) and pneumatic spray pyrolysis (PSP) techniques. HRTEM on the NPs shows difference in lattice spacing in the NP structures prepared by the two methods—2.02 Å for the USP NPs and an average of 3.74 Å for the PSP NPs. The most probable particle sizes are 3.11 nm and 5.5 nm, respectively. Raman spectroscopy supported by FTIR confirms the TiO₂ polymorph to be anatase with the intense phonon frequency at 153 cm⁻¹ blue-shifted from 141 cm⁻¹ ascribed to both carbon doping and particle size. A modified phonon confinement model for nanoparticles has been used to extract phonon dispersion and other parameters for anatase for the first time. Electronic measurements show “negative conductance” at some critical bias voltage, which is characteristic of *n*-type conductivity in the carbon-doped TiO₂ NPs as confirmed by the calculated areas under the *I*-*V* curves, a property suited for solar cell applications. Practical solar cells built from carbon-doped TiO₂ electrodes show up to 1.5 times improvement in efficiency compared to pure TiO₂ electrodes of similar construction.

1. Introduction: Efficiency Improvement Efforts on Dye Solar Cells

Various tables reporting figures of efficiency for different types of solar cells have been released several times by different groups. But the most up-to-date chart has been released by the National Renewable Energy Laboratory [1]. The chart shows that efficiency values for all solar cell types are steadily increasing from the earliest reported levels in the 1970s and 1980s. The highest values from 16–41% are found in multijunction concentrators GaAs with the latest (2007) figure of 41% reported by Boeing. Crystalline silicon cells range from 16–24%, multicrystalline Si from 12–18%, thin-film solar cells containing either Cu(In,Ga)Se₂ or CdTe

or amorphous SiH or nano-Si or micro-Si or poly-Si or multijunction Si ranging from 1–17%. The rapid increase in efficiency in nano-Si from about 8% in 1997 to 14% in 2001 demonstrates the importance of nanotechnologies in the improvement of the solar cells level of efficiency. Dye-sensitized solar cells (DSSCs) with a range of 5% in 1991 to 11% in 2006 have nearly the lowest range with the partners—the organic solar cells—at the lowest end of 1% in 2001 to 5.4% in 2006.

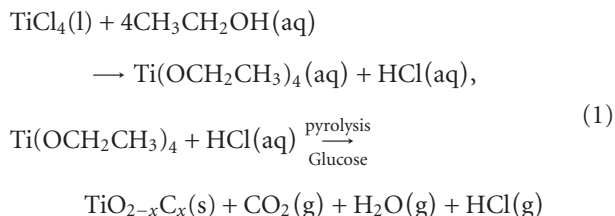
Solar cell types displaying the highest efficiency figures are difficult to produce due to material processing costs such as in silicon and GaAs alloys or precursor toxicity such as in selenides and sulfides and hence expensive [2]. These disadvantages are not an issue in low efficient types such as

the organic ones and the dye-sensitized cells. For the reasons of nontoxicity and the possibility of mass production from low-cost starting materials, it is wise to study the materials properties for the emerging solar cell types especially the dye-sensitized one. The discovery of the pertinent properties that would drastically raise the efficiency of DSSCs will be very indispensable. The DSSCs, the Grätzel cells, consist of thin films of *n*-type titanium dioxide (TiO₂) coated with a ruthenium metal organic dye [3]. They offer easy processing and can attain new roles over conventional silicon solar cells. Generally, the ways explored to improve the efficiency of DSSCs have focused on upgrading the components of the solar cell to enhance photovoltage (*V*_{OC}) by varying (a) the supporting oxide, (b) the electrolyte which stabilizes the solar cell, and (c) the dyes which enhance the photocurrent [4, 5]. Carbon in DSC electrodes has gained attention recently, for instance, flexible C to complete with Pt:FTOs [6], C:TiO₂ for photocatalysis [7–9].

We report on the optical, structural, and electronic properties of TiO₂ NPs when doped with carbon (C:TiO₂ NPs) synthesized by spray pyrolysis and how that C:TiO₂ NPs increase the visible light absorption coefficient. These C:TiO₂ NPs are tested in DSSCs.

2. Experimental: Preparation and Characterization of Carbon Modified TiO₂

The proposed reaction sequence for the production of C:TiO₂ NPs, similar to that proposed by Livage [10] in the production of vanadium ethoxide and Mwakikunga et al. [11] in the production of tungsten ethoxide, is as follows:



C:TiO₂ NPs were synthesized by USP and PSP. The schematics for USP and PSP are given in Figure 1.

The USP technique involves focusing ultrasound waves of frequency *F* producing capillary waves of frequency *f*_{USP} at the surface of the precursor liquid. This produces ultrafine droplets of the precursor liquid. The ultrasonic nebulizer uses an ultrasound generator to drive a piezoelectric crystal at a fixed frequency, *F*. The surface of the liquid will break down when the longitudinal waves propagate from the crystal to the liquid-air interface. The PSP involves blowing the precursor liquid through fine nozzles to produce a mist of the precursor liquid at audible sound and ultrasonic frequencies, *f*_{PSP}. In both cases, the precursor droplets were generated in a chamber that was housing the nebulizer. The vapors generated are transported to a heated zone through a quartz tube onto glass substrate precoated with a transparent conducting layer of F:SnO₂ placed inside a furnace. The spray deposition is carried out for an hour. The wavelength of the capillary waves

is expressed as $\lambda = (8\pi\sigma/\rho \cdot f^2)^{1/3}$ where σ and ρ are the surface tension and density of the liquid, which, for high enough intensity of the forcing sound, erupt into droplets of mean diameter $D_{\text{USP}} = (8\pi\sigma/\rho \cdot f_{\text{USP}}^2)^{1/3}$ and $D_{\text{PSP}} = (8\pi\sigma/\rho \cdot f_{\text{PSP}}^2)^{1/3}$ respectively. After decomposition and deposition in the pyrolysis process, the solid-state particles obtained have mean diameter that can be estimated respectively as $d_{\text{USP}} = (D_{\text{USP}}(C_{\text{pr}}M_{\text{p}})/(\rho_{\text{p}}M_{\text{pr}}))^{1/3}$ and $d_{\text{PSP}} = (D_{\text{PSP}}(C_{\text{pr}}M_{\text{p}})/(\rho_{\text{p}}M_{\text{pr}}))^{1/3}$ where C_{pr} is the concentration of the precursor, M_{pr} and M_{p} are the molar masses of the precursor and deposited particles respectively; and ρ_{p} and ρ_{pr} are the densities of the deposited particles and precursor liquid respectively [12–15].

An aliquot of 0.1 M precursor solution of titanium ethoxide was prepared by adding 11.8825 g of titanium tetrachloride (TiCl₄) and 0.2162 g of glucose into a 250 mL volumetric flask in absolute ethanol (99.99%, Aldrich). The solution was then mixed vigorously till all the glucose particles were not visible. The precursor solution was then decanted into (1) a chamber that was housing the ultrasonic nebulizer operating at a frequency of 1.67 MHz for USP and (2) into tube connected to a pneumatic pump for PSP. F:SnO₂ transparent glass substrates were first washed with detergent then thoroughly rinsed with distilled water, isopropanol, distilled water and finally acetone. The glass substrates were then dried under hot air to evaporate the acetone. Nano-particle deposition was done on F:SnO₂ glass substrate at furnace temperatures of 450–455°C, at various substrate positions inside the furnace using argon as the carrier gas at a flow rate of 5.5 mL/min. Structural studies of the as deposited nano-particles were done using a Philips XPert powder X-ray diffractometer with a CuK_α wavelength of 0.154184 nm. High resolution transmission electron microscopy (HRTEM) performed on a Jeol JSM 2100 was used to determine structure—lattice parameters—of the C:TiO₂ NPs; the HRTEM was also equipped with the energy dispersive X-ray spectroscopy (EDXS) setup using a Thermo Fisher Scientific detector cooled at liquid nitrogen temperature. Optical characterization (Diffuse reflectance spectra) was done using a Varian Cary Uv-Vis-IR spectrometer in the wavelength range of 250–2000 nm.

Raman spectroscopy (RS) was carried out using a Jobin-Yvon T64000 Raman spectrograph with a 514.5 nm line from an argon ion laser. The power of the laser at the sample at the post-annealed samples was small enough (0.384 mW) in order to minimise localised heating of the sample. The T64000 was operated in single spectrograph mode, with the 1800 lines/mm grating and three objective lenses on the microscope with the following magnifications: 20x, 50x and 100x.

Fourier Transform Infrared (FTIR) spectra of both pure and carbon modified titanium dioxide samples were carried out in the 350–4000 cm⁻¹ frequency range. The infrared absorption spectra were recorded on Nicolet Nexus 870 system FTIR spectrometer at room temperature. Dried solid samples were pressed with KBr (FT-IR grade Aldrich) and pellets were scanned 34 times using transmission mode with a resolution of 4 cm⁻¹.

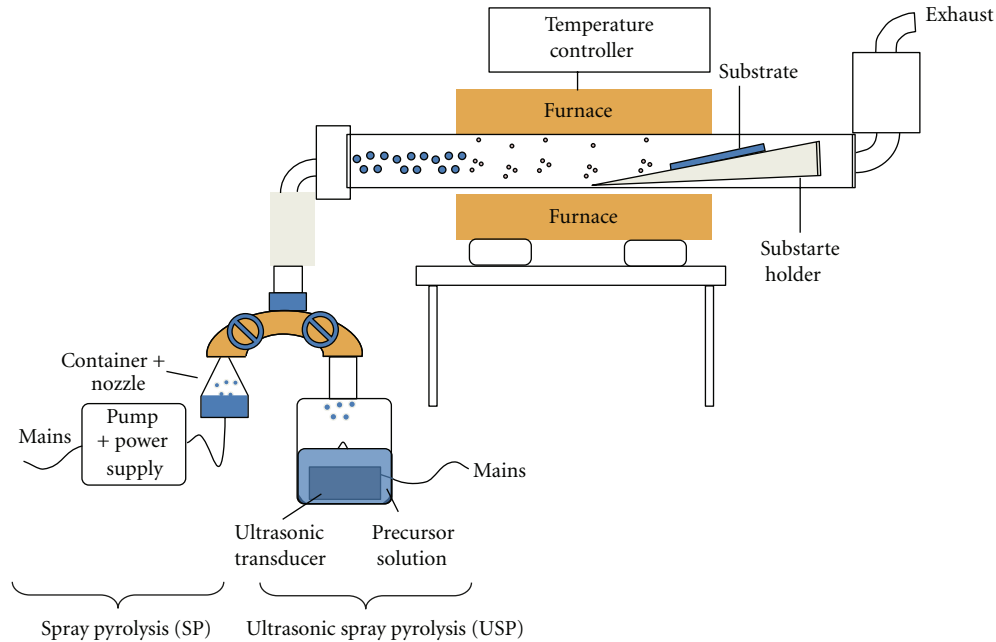


FIGURE 1: Schematic setup of pneumatic spray pyrolysis (PSP) and ultrasonic spray pyrolysis (USP).

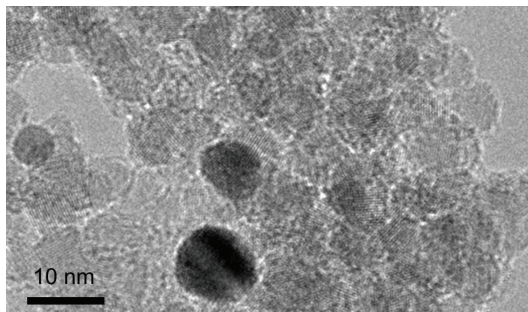


FIGURE 2: HRTEM image C:TiO₂ QDs growing by PSP.

A colinear four-point probe system from Cascade Microtech, Inc., Oregon, USA was used to perform conductance measurements on the C:TiO₂ NPs. The equidistant tungsten carbide probes have a separation distance, a , of 0.127 cm and a probe radius of 0.005 cm. The Keithley 4200 semiconductor characterization system (SCS), equipped with four supply-and-measure units (SMUs) and a pre-amplifier, was used to perform high-precision direct-current characterization capable of probing-sensitive voltages and injecting currents ranging from 1 fA–1 mA with a resolution of 0.1 fA. In this work, a current was injected through two extreme probes through the sample. The potential difference was measured across the middle probes.

3. Structural Properties of the Carbon-Modified TiO₂ Anatase

The lower magnification HRTEM showed that for the PSP prepared sample the particles were mostly spherical and had

mean diameter of 5.5 nm. The same can be said of the USP prepared sample only the particle size is smaller (Figure 2). In this case, the mean diameter is 3.11 nm. The EDXS of these PSP synthesized C:TiO₂ NPs (not shown) showed presence of Ti, O and C only signifying the purity of the obtained material. Cu peaks and some C intensity came from the carbon-hole copper grids used in these experiments.

TiO₂ exists in the following known polymorphs: anatase ($a = 3.784 \text{ \AA}$, $c = 9.514 \text{ \AA}$, $\alpha = \beta = \gamma = 90^\circ$ PDF# 78–2486) with the strongest d -spacing of 3.52 \AA [16], rutile ($a = 4.593 \text{ \AA}$, $c = 2.958 \text{ \AA}$, $\alpha = \beta = \gamma = 90^\circ$ PDF# 89-8304) with a d -spacing of 3.25 \AA [17] brookite ($a = 9.174 \text{ \AA}$, $b = 5.449 \text{ \AA}$, $c = 5.138 \text{ \AA}$, $\alpha = \beta = \gamma = 90^\circ$ PDF# 76-1934) with a d -spacing of 3.51 \AA [18] and hongquite ($a = 4.173 \text{ \AA}$, $\alpha = \beta = \gamma = 90^\circ$ PDF# 89-3660) with a d -spacing of 2.09 \AA [19].

The higher magnification HRTEM clearly reveals that USP TiO₂ NPs have a very small d -spacing compared to the normal anatase spacing of 0.352 nm . The d -spacing found in this sample is about 0.202 nm as shown Figure 3.

However, the PSP C:TiO₂ NPs have a distribution of interplanar d -spacings whose distribution is given in Figure 4(b) indicating that some particles have their d -spacings less or more than 0.352 nm . In fact, most of the particles have most probably d -spacing of 0.374 nm in agreement with the anatase TiO₂ as found by Bersani et al. [17]. It has been observed, especially in ZnO, that carbon doping, where C substitutes O, tends to reduce the d -spacing of the C:ZnO. It can, therefore, be concluded that those C:TiO₂ NPs that show larger d -spacings than the anatase observed in PSP samples have interstitial carbon doping as presented in Figure 4. The lower d -spacings suggest substitutional C doping as seen in some particles in the PSP sample and in almost all the particles in the USP sample.

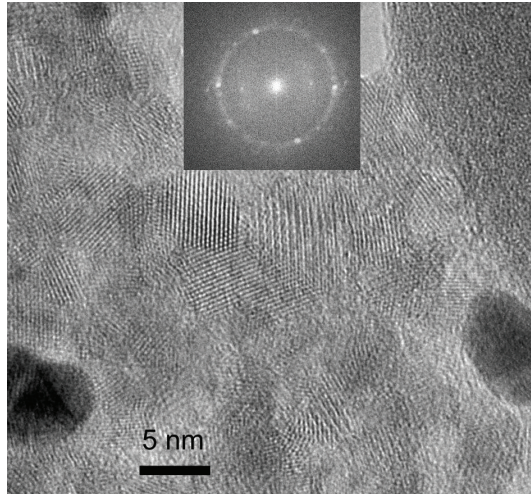


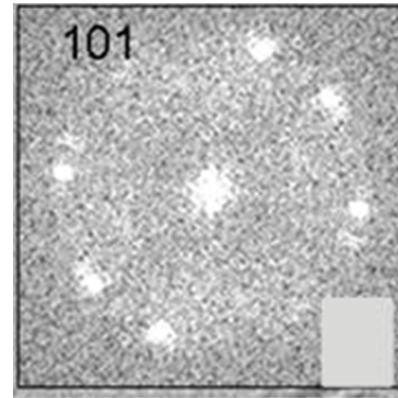
FIGURE 3: HRTEM of the USP C:TiO₂ QDs evident with a fringe separation of 2.017 Å. Inset is the FFT of the high-resolution image showing the reflection from the predominant (101) plane of the TiO₂ lattice.

We can, therefore, speculate that USP is a more efficient technique for incorporating carbon uniformly in the TiO₂ matrix. On the other hand, such a large change in lattice spacing, compounded with the large distribution shown in Figure 4(b) cannot be entirely due to carbon doping. This can be attributed to the fact there are various types of crystallites in the intrinsic TiO₂ material itself. Therefore, we can conclude this is a polycrystalline material.

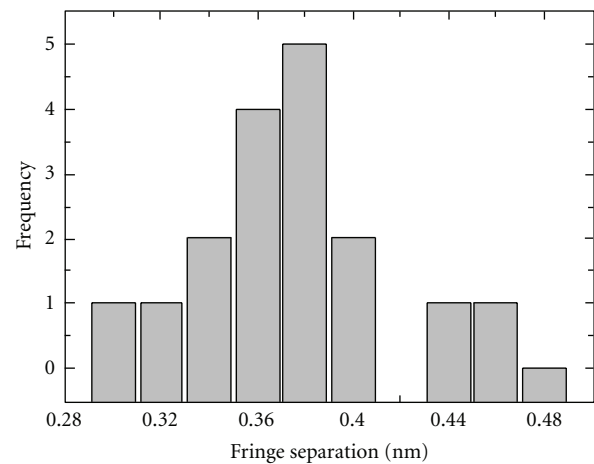
The fast Fourier transform (FFT) of the images, synonymous to the selected area electron diffraction, displays the fact that only the main diffraction (reflection) plane of Miller indices (101) in TiO₂ [17] is responsible for diffraction pattern. In the PSP sample, the particles with the same Miller indices are oriented in different direction. This is why their spots on the FFT image (Figure 4 inset a) give a circle of uniform radius, which is indexed to the (101) plane. However, in the USP sample, the particles tend to show similar orientation with one direction on the FFT image (Figure 3(b)).

4. Phonons in the C_xTiO_{2-x} Alloy

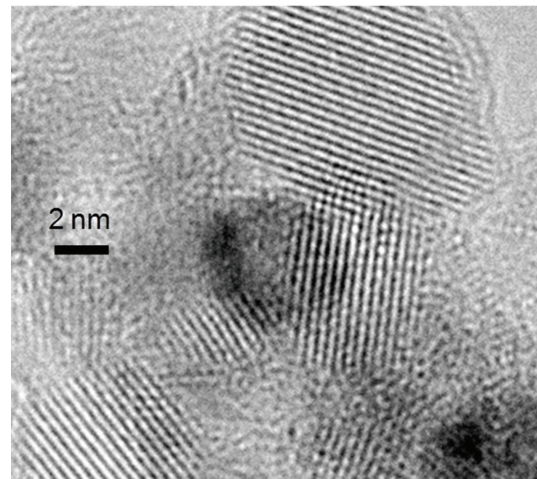
The FTIR spectra for pure unannealed TiO₂ (Pure TiO₂ spot 1 in Figure 5), pure annealed TiO₂ at 500°C (pure TiO₂ spot 2 in Figure 5), and carbon modified TiO₂ samples display significant differences: (1) the splitting of the main Ti-O phonon (at 664 cm⁻¹) into two—one at 659 cm⁻¹ and another at 536 cm⁻¹ and (2) the emergence of new absorption peaks in the range from 1400 to 1600 cm⁻¹. The phonon splitting can be assigned to surface phonons due to small particle size whereas the new peaks in the range from 1400 to 1600 cm⁻¹ can be due to the presence of carbon in the particle as shown in the enlarged inset of Figure 5. There is no indication of the structure of the carbon dopant with the



(a)



(b)



(c)

FIGURE 4: HRTEM of the PSP C:TiO₂ QDs. Inset (a) is the FFT of the high-resolution image showing the reflection from the predominant (101) plane of the TiO₂ lattice from a number of particles in the high-resolution image and inset (b) is the fringe separation distribution histogram of the PSP C:TiO₂ QDs.

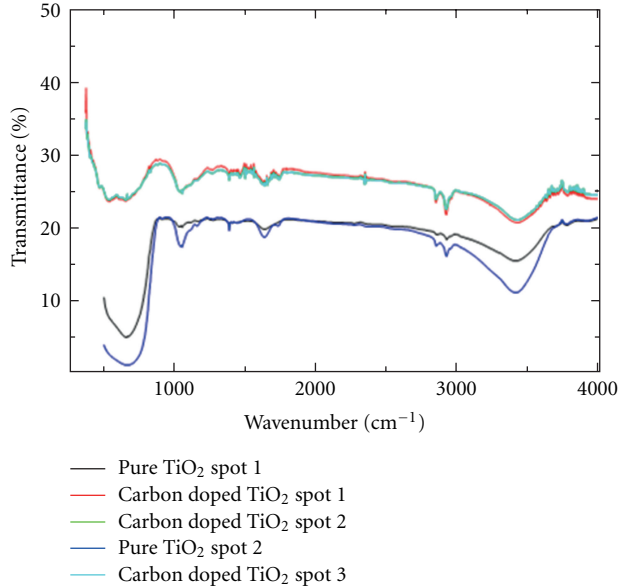
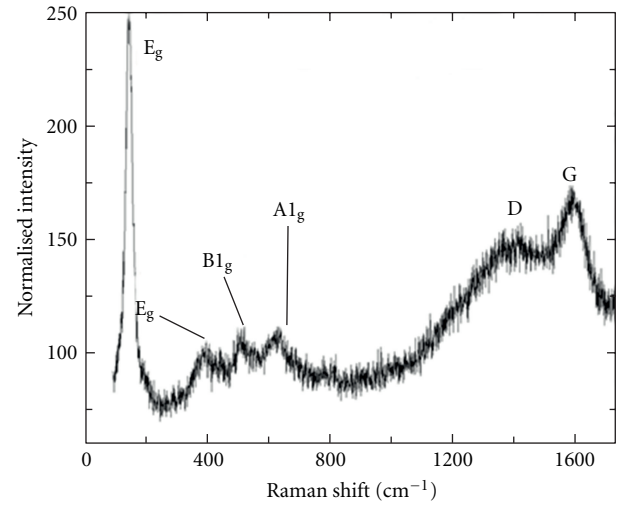


FIGURE 5: FTIR spectroscopy of pure TiO_2 compared with C:TiO₂ QDs synthesized by PSP technique.

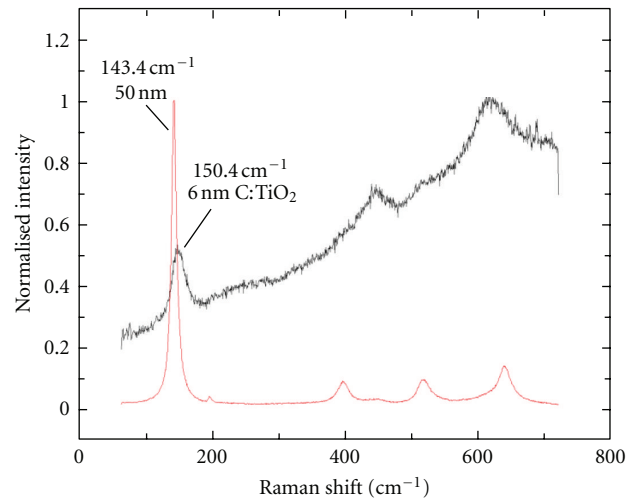
present FTIR spectra. However, these peaks are ably captured in Raman spectroscopy presented herein.

TiO_2 is known to exhibit six Raman active bands characteristic of anatase phase at 144, 197, 399, 515, 519, and 639 cm^{-1} with symmetries of E_g , E_g , B_{1g} , A_{1g} , B_{1g} , and E_g respectively [20–22]. However, it has been shown [23] that, when TiO_2 are coated with carbon as core-shell particles, the main E_g mode of 144 cm^{-1} blue shifts to $\sim 153 \text{ cm}^{-1}$. This is what we see in our typical Raman spectrum for the PSP sample where this phonon mode has shifted to 152 cm^{-1} . Raman spectroscopy in this case suggests carbon doping in our samples. We have extended our RS to include the carbon bands as shown in Figure 6(a). We observed the D-band of the disordered carbon at 1354 cm^{-1} and the perfect graphite peak at 1583 cm^{-1} [23, 24]. This is a clear indication of the presence of carbon in these samples, which supports the HRTEM results in this work. Raman spectroscopy of the C:TiO₂ NPs also shows broadening and blue shift of the anatase E_g phonon lineshape (Figure 6(b)) when compared to bulk TiO_2 of mean size of 50 nm. This lineshape is also asymmetrical (Figure 6(c)) which is an indication that either there is optical phonon confinement or the inhomogeneous laser heating effects on the TiO_2 nanostructures [24, 25] or both.

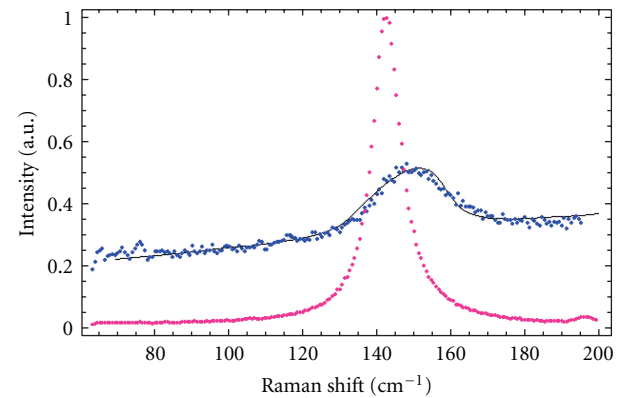
In order to pursue phonon confinement, it is important to lay a brief background. In the 1980s, it became apparent that Raman spectral line shapes for microcrystals could not follow the perfect Gaussian profile [26]. It was then realised that there was need for a deeper understanding of the origin of this asymmetry. Spatial correlation modelling, as it was called, then became one way to extract information from RS data. It was stated in our previous work [27] that the justification for this new behavior is that, for a perfect (bulk) crystal of diameter d having vibrational modes of momentum \mathbf{q} ,



(a)



(b)



(c)

FIGURE 6: Raman spectroscopy of the C:TiO₂ QDs synthesized by PSP technique showing (a) the presence of carbon D and G bands in the 6-nm QDs, (b) the major anatase peak at 153 cm^{-1} shifted from the pure bulk TiO_2 peak at 143 cm^{-1} , and (c) the present confinement model fitted to the 6-nm particles data.

the Heisenberg's uncertainty principle ($\delta d \cdot \delta \mathbf{q} \sim h$) means that as $\delta d \rightarrow \infty$ (bulk) then $\delta \mathbf{q} \rightarrow 0$ (the " $\mathbf{q} = 0$ " selection rule applies). As the diameter, $\delta d \rightarrow 0$ (nanometric) then the vibrational momentum, $\mathbf{q} \rightarrow \infty$. In this case, the " $\mathbf{q} = 0$ " selection rule breaks down; a contribution from the $\mathbf{q} \neq 0$ phonons determined by the dispersion relation $\omega \mathbf{q}$ is allowed [27]. This accounts for the asymmetric broadening of the peaks in a Raman spectrum. The Richter equation for confined phonons in spherical nanoparticles [26] was modified to include Gaussian distribution of the phonon momenta and particle size by Bhattacharyya and Samui [28] and given here as

$$I(\omega) = A_0 \int_{-\infty}^{\infty} \left[\frac{|C(0, \mathbf{q})|^2}{(\omega - \omega(\mathbf{q}))^2 + (\Gamma_0/2)^2} \right] d^3 \mathbf{q}, \quad (2)$$

In the equation, Γ_0 is the full-width-at-half-maximum (FWHM) for bulk material Raman peak (for instance $\Gamma_0 = 7.0 \text{ cm}^{-1}$ for bulk TiO_2 [29]), $\omega \mathbf{q}$ is the phonon dispersion curve relation (PDR) for the material (e.g. $A = 145 \text{ cm}^{-1}$, $a = 0.32 \text{ nm}$ for the 144 cm^{-1} phonon branch). The Richter et al. model is valid for spherical nanocrystals of mean diameter L for which the Fourier coefficient $C(0, \mathbf{q})$ was assumed to be Gaussian of the form $\exp(-\mathbf{q}^2 L^2 / 4\pi^2)$ with a phonon amplitude at the boundary of $1/e$. When geometry deviates from a sphere, then adjustment has to be carried out. And so, we fit the following equation to the 6 nm mean diameter nanoparticles:

$$I(\omega) = A_1 + m\omega + A_0 \int_{L_{\min}}^{L_{\max}} dL \times \rho(L) \int_{-\infty}^{\infty} \left[4\pi \mathbf{q}^2 \frac{\exp(\mathbf{q}^2 L^2 / \alpha)}{(\omega - \omega_0 \pm B a \mathbf{q}^2)^2 + (\Gamma_0/2)^2} \right] d\mathbf{q}. \quad (3)$$

The fitting was performed by activating a "Statistics NonlinearFit" routine in Mathematica 4.1 and is presented graphically in Figure 6(c). From this fit, the following parameters are extracted $A_0 = 10^{-17}$, $\alpha = 3 \pi^2$ (~ 30), $\omega_0 = 150.4 \text{ cm}^{-1}$, $B = 0.005 \text{ cm}^{-2}$, and $\Gamma_0 = 20 \text{ cm}^{-1}$. Note that the value of 20 cm^{-1} for Γ_0 is 13 cm^{-1} above the value for bulk TiO_2 . Also the size distribution integral in (3) has been replaced by an expression $A_1 + m\omega = 0.25 + 0.008\omega$ to take into account the background noise inherent in the fluorescent nanostructures. These results show that the blue shift of the central Brillouin zone phonon frequency from 143.4 cm^{-1} for particles of mean diameter of 50 nm of pure TiO_2 to 150.4 cm^{-1} for particles of mean diameter of 6 nm is not only due to reduction of particle size but also could be due to the presence of carbon in the TiO_2 structure. We are yet to determine the singular contribution of carbon doping to this blue shift.

5. Optical Properties of the Carbon-Modified TiO_2

It is well known that pure TiO_2 can only absorb light below the wavelength of 387.5 nm because its bandgap is 3.2 eV.

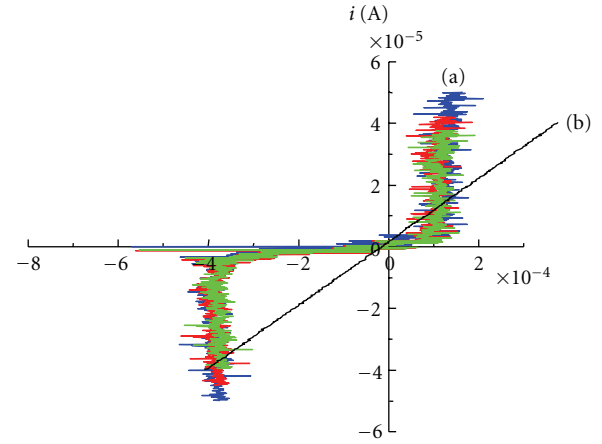


FIGURE 7: Current-Voltage characteristics for the transparent ohmic conductor F:SnO₂ on glass substrate (line (b)) showing ohmic behaviour and the C:TiO₂ QDs (curves (a)) showing semiconductor behaviour.

In order to extend the absorption region of TiO_2 to use the majority of the sunlight of the solar spectrum, doping of titanium dioxide with nonmetal, transition metals, and composite transition metal oxide has been employed [30–35]. Doping of TiO_2 inhibits recombination of photogenerated electrons and holes by increasing the charge separation and, therefore, enhances the efficiency of photon generation [30]. Carbon has been found to be a suitable dopant for TiO_2 , in applications that involve solar energy conversion. The presently carbon-doped TiO_2 samples showed a strong and broad absorption band around 637 nm in the UV-Vis-IR spectra (not shown). The solar emission spectrum ranges from 250 nm to 2500 nm. The shift in the absorption from below 387.5 nm (pure TiO_2) to 637 nm (C:TiO₂ NPs) is a positive indication that the C:TiO₂ samples will perform different in a solar cell.

6. Current-Voltage Output Characteristics of the Alloy

Figure 7 shows the I - V characteristics of the C:TiO₂ NPs. The four-point probe I - V curve characteristic of F:SnO₂ on the glass substrate is shown in Figure 7(b) with a voltage sweep from -0.4 mV to 0.4 mV . The I - V curve shows that there is a linear relationship between current and voltage where $I \sim \sigma \cdot V$ (σ being the conductance) and it also shows that the F:SnO₂ on the glass substrate is indeed a transparent ohmic conductor. Typical I - V characteristics of C:TiO₂ NPs deposited on FTO glass substrate are shown in Figure 6(a) with a current sweep in the range of $-60 \mu\text{A}$ to $+60 \mu\text{A}$. The measurements from different spots gave slightly different values, which is caused by inhomogeneous deposition of the nanoparticles onto the glass substrates during spray pyrolysis. However, there is a general similarity of the I - V curves for the different spots.

On all spots of the C:TiO₂ NPs film, the I - V curves clearly suggest that the NPs are semiconducting with a bandgap (E_g)

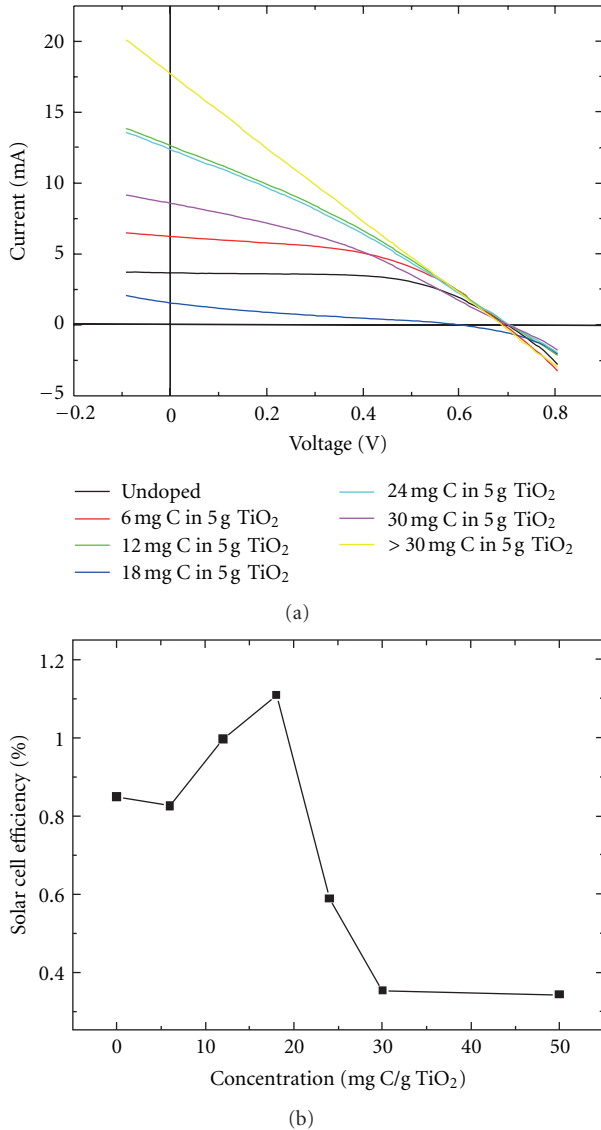


FIGURE 8: I-V characteristics of the typical dye sensitized solar cells containing varying mg of carbon in the TiO₂ as electrode (b) Efficiency of such solar cells as a function of carbon concentration.

determined from the width of the I - V curve when current is nearly zero. The bandgap here expressed in volts is found to be about 4×10^{-4} V. Extracalibration is required to convert this reading into electron volts (eV). This is beyond the scope of this paper. However, this value could be comparable to the band gap of TiO₂ of 3.2 eV found by other methods. The deviation of the E_g from 3.2 eV should be proportional to the amount of carbon doping and also particle size.

Also from the I - V curves one could speculate the type of conductivity one gets in the C:TiO₂ NPs. TiO₂ is naturally n -type semiconductor. Doping with carbon is expected to increase the electron density and make it more n -type.

The I - V characteristics in the $(-x, -y)$ quadrant of Figure 7 clearly indicates a negative slope which suggests “negative conductance.” This apparent negative conductance

could be due to the so-called Gunn effect which was discovered in III-V compounds such as GaAs and InP and reported by Gunn in 1963 [33]. Gunn saw that when an electric field reaches a threshold value in some materials the mobility of electrons decreases as the electric field is increased further, thereby producing negative resistance. Other authors such as Shikwambana et al. [36] and Mwakikunga et al. [37, 38] have reported S-shaped I - V curves in VO₂ which show negative conductance. At a critical current, a core of the low resistivity phase was seen to be formed and this was attributed to the falling of the voltage across the device while the current increased to a value dependent on a specific load line. With further increases in the circuit current, the voltage across the device was seen to decrease slightly. Also the role of doping on the negativity of the slope in the I - V curves have been reported in boron-doped diamond [38] pointing this phenomenon to the n -type conductivity of these type of diamonds.

Furthermore, by inspection, the I - V curves are not symmetrical about the $V = 0$ point but rather shifted to negative voltages such that if one fits some analytical function $i(V)$ such as Shockley’s diode equation among others and calculates the area under the I - V curves in the negative voltage and positive voltage sections, one can state that

$$\text{If } \int_{-V}^0 i(V)dV > \int_0^V i(V)dV \quad \text{then } n\text{-type} \\ \text{else } p\text{-type.} \quad (4)$$

The integral of $i(V)dV$ calculates the total electrical energy dissipated on charge carriers. The principle in (4) states that if more electrical energy is spent on driving the negative charge carriers in a semiconductor then such a material is intrinsically n -type and vice versa. From the curves in Figure 7, 20 nW are spent on electrons whereas only 5 nW are spent on the holes. We sufficiently concluded that our carbon-doped TiO₂ NPs are indeed n -type which is a necessary precursor for planned DSSC electrode.

7. TiO₂ Electrodes of Carbon-Dopant Concentration Used in the Dye-Sensitised Solar Cells

With the carbon doped TiO₂ electrode results, we continued to build dye-sensitized solar cells containing TiO₂ electrodes of varying carbon-dopant concentrations. This concentration is calculated from the amount of sucrose in mg for every litre of the total volume of the precursor material. The solar cell area was kept constant at 1.8 cm². The current-voltage characteristics of each individual cell are presented in Figure 8(a). Efficiency values were calculated from open-circuit voltage values and short-circuit current obtained from these current-voltage output characteristics. The efficiency values at varying carbon concentration are given in Figure 8(b). The current efficiency values (~ 0.3 – 1.1%) are admittedly much lower than those obtained for dye sensitized solar cells (~ 5 – 11%). This can be improved by employing more careful fabrication processes. However, the current results, at the laboratory scale, show that

carbon concentration does increase the efficiency of the dye-sensitized solar cell by about 1.5 times over the solar cell with pristine TiO₂ layer.

8. Conclusion

We have successfully synthesized C:TiO₂ NPs using ultrasonic nebulizer spray pyrolysis (USP) and pneumatic spray pyrolysis (PSP) techniques. These spherical nanoparticles have a modal particles size of 3.11 nm and 5.5 nm, respectively. The lattice fringe separations are 2.017 Å for USP and 3.74 Å for PSP. This suggests substitutional carbon doping for USP and a mixture of substitutional and interstitial carbon doping for PSP. In both processes, the TiO₂ structure changes with the most predominant reflection plane of (101) of the TiO₂ observed. The Raman active phonon of 141 cm⁻¹ from anatase is shifted to 150.4 cm⁻¹ due to both size effect and carbon doping in agreement with most previous findings. The carbon doping enhanced the TiO₂'s *n*-type conductivity with the *I*-*V* characteristics manifesting "negative conductance" especially when negative voltage is used. The *n*-type conductivity has also been confirmed by calculating areas under the *I*-*V* curves. The C:TiO₂ NPs produced in this study show properties that would not only make the materials suitable for photocatalytic activity, but also for electrodes in Grätzel-type of solar cells. Efficiency values for solar cells of varying carbon concentrations in their TiO₂ electrodes show up to 1.5 times improvement over the pure TiO₂ electrode-based solar cells.

Acknowledgments

Financial support from our sponsors, SANERI, ESKOM, and Govan Mbeki R&D Centre at the University of Fort Hare, is acknowledged. The authors are thankful for infrastructural support from Ithemba LABS (Gauteng,) and DST/CSIR National Centre for Nano-Structured Materials. Additional financial support from the India-Brazil-South Africa (IBSA) programme is also acknowledged.

References

- [1] "Reported timeline of solar cell energy conversion efficiencies," National Renewable Energy Laboratory (USA), [http://en.wikipedia.org/wiki/File:Pveff\(rev110707\)d.png](http://en.wikipedia.org/wiki/File:Pveff(rev110707)d.png).
- [2] M. Grätzel, "Molecular photovoltaics that mimic photosynthesis," *Pure and Applied Chemistry*, vol. 73, no. 3, pp. 459–467, 2001.
- [3] J. He, H. Lindström, A. Hagfeldt, and S. E. Lindquist, "Dye-sensitized nanostructured tandem cell-first demonstrated cell with a dye-sensitized photocathode," *Solar Energy Materials and Solar Cells*, vol. 62, no. 3, pp. 265–273, 2000.
- [4] J. Bandara and H. Weerasinghe, "Design of high-efficiency solid-state dye-sensitized solar cells using coupled dye mixtures," *Solar Energy Materials and Solar Cells*, vol. 90, no. 7-8, pp. 864–871, 2006.
- [5] K. T. Roro, B. Mwakikunga, N. Tile, B. Yalisi, and A. Forbes, "Effect of accelerated thermal ageing on the selective solar thermal harvesting properties of multiwall carbon nanotube/nickel oxide nanocomposite coatings," *International Journal of Photoenergy*, vol. 2012, Article ID 678394, 7 pages, 2012.
- [6] J. Chen, K. Li, Y. Luo et al., "A flexible carbon counter electrode for dye-sensitized solar cells," *Carbon*, vol. 47, no. 11, pp. 2704–2708, 2009.
- [7] G. Jiang, Z. Lin, L. Zhu, Y. Ding, and H. Tang, "Preparation and photoelectrocatalytic properties of titania/carbon nanotube composite films," *Carbon*, vol. 48, no. 12, pp. 3369–3375, 2010.
- [8] H. Wang, X. Quan, H. Yu, and S. Chen, "Fabrication of a TiO₂/carbon nanowall heterojunction and its photocatalytic ability," *Carbon*, vol. 46, no. 8, pp. 1126–1132, 2008.
- [9] R. Leary and A. Westwood, "Carbonaceous nanomaterials for the enhancement of TiO₂ photocatalysis," *Carbon*, vol. 49, no. 3, pp. 741–772, 2011.
- [10] J. Livage, "Vanadium pentoxide gels," *Chemistry of Materials*, vol. 3, no. 4, pp. 578–593, 1991.
- [11] B. W. Mwakikunga, A. Forbes, E. Sideras-Haddad, M. Scriba, and E. Manikandan, "Self assembly and properties of C:WO₃ nano-platelets and C:VO₂/V₂O₅ triangular capsules produced by laser solution photolysis," *Nanoscale Research Letters*, vol. 5, no. 2, pp. 389–397, 2010.
- [12] B. W. Mwakikunga, E. Sideras-Haddad, and M. Maaza, "First synthesis of vanadium dioxide by ultrasonic nebula-spray pyrolysis," *Optical Materials*, vol. 29, no. 5, pp. 481–487, 2007.
- [13] B. W. Mwakikunga, E. Sideras-Haddad, A. Forbes, and C. Arendse, "Raman spectroscopy of WO₃ nano-wires and thermo-chromism study of VO₂ belts produced by ultrasonic spray and laser pyrolysis techniques," *Physica Status Solidi*, vol. 205, no. 1, pp. 150–154, 2008.
- [14] B. W. Mwakikunga, E. Sideras-Haddad, C. Arendse, M. J. Witcomb, and A. Forbes, "WO₃ nano-spheres into W₁₈O₄₉ one-dimensional nano-structures through thermal annealing," *Journal of Nanoscience and Nanotechnology*, vol. 9, no. 5, pp. 3286–3294, 2009.
- [15] B. W. Mwakikunga, A. Forbes, E. Sideras-Haddad, and C. Arendse, "Optimization, yield studies and morphology of WO₃ nano-wires synthesized by laser pyrolysis in C₂H₂ and O₂ ambients-validation of a new growth mechanism," *Nanoscale Research Letters*, vol. 3, no. 10, pp. 372–380, 2008.
- [16] E. P. Meagher and G. A. Lager, "Polyhedral thermal expansion in the TiO₂ polymorphs: refinement of the crystal structures of rutile and brookite at high temperature," *The Canadian Mineralogist*, vol. 17, pp. 77–85, 1979.
- [17] D. Bersani, P. P. Lottici, and X.-Z. Ding, "Phonon confinement effects in the Raman scattering by TiO₂ nanocrystals," *Applied Physics Letters*, vol. 72, no. 1, p. 73, 1998.
- [18] D. Luca and L. S. Hsu, "Structural evolution and optical properties of TiO₂ thin films prepared by thermal oxidation of PLD Ti films," *Journal of Optoelectronics and Advanced Materials*, vol. 5, no. 4, pp. 835–840, 2003.
- [19] R. Suthyanoorthy, P. Sudhagar, S. Chadramohan, and K. P. Vijayakumar, "Photoelectrical properties of crystalline titanium dioxide thin films after thermo-annealing," *Crystal Research and Technology*, vol. 42, no. 5, pp. 498–503, 2007.
- [20] X. Hu, T. Zhanga, Z. Jina et al., "Fabrication of carbon-modified TiO₂ nanotube arrays and their photocatalytic activity," *Materials Letters*, vol. 62, no. 30, pp. 4579–4581, 2008.
- [21] G. Katumba, B. W. Mwakikunga, and T. R. Mothibinyane, "FTIR and Raman spectroscopy of carbon nanoparticles in SiO₂, ZnO and NiO matrices," *Nanoscale Research Letters*, vol. 3, no. 11, pp. 421–426, 2008.

- [22] S. Piscanec, M. Cantoro, A. C. Ferrari et al., "Raman spectroscopy of silicon nanowires," *Physical Review B*, vol. 68, no. 24, Article ID 241312, 4 pages, 2003.
- [23] H. Richter, Z. P. Wang, and L. Ley, "The one phonon Raman spectrum in microcrystalline silicon," *Solid State Communications*, vol. 39, no. 5, pp. 625–629, 1981.
- [24] I. H. Campbell and P. M. Fauchet, "The effects of microcrystal size and shape on the one phonon Raman spectra of crystalline semiconductors," *Solid State Communications*, vol. 58, no. 10, pp. 739–741, 1986.
- [25] K. R. Zhu, M. S. Zhang, Q. Chen, and Z. Yin, "Size and phonon-confinement effects on low-frequency Raman mode of anatase TiO₂ nanocrystal," *Physics Letters A*, vol. 340, no. 1–4, pp. 220–227, 2005.
- [26] D. Wang, J. Zhao, B. Chen, and C. Zhu, "Lattice vibration fundamentals in nanocrystalline anatase investigated with Raman scattering," *Journal of Physics: Condensed Matter*, vol. 20, no. 8, Article ID 085212, 2008.
- [27] C. Xu, Y. A. Shaban, W. B. Ingler, and S. U. M. Khan, "Nanotube enhanced photoresponse of carbon modified (CM)-n-TiO₂ for efficient water splitting," *Solar Energy Materials and Solar Cells*, vol. 91, no. 10, pp. 938–943, 2007.
- [28] S. Bhattacharyya and S. Samui, "Phonon confinement in oxide-coated silicon nanowires," *Applied Physics Letters*, vol. 84, no. 9, p. 1564, 2004.
- [29] Y. A. Shaban and S. U. M. Khan, "Surface grooved visible light active carbon modified (CM)-n-TiO₂ thin films for efficient photoelectrochemical splitting of water," *Chemical Physics*, vol. 339, no. 1–3, pp. 73–85, 2007.
- [30] V. Keller and F. Garin, "Photocatalytic behavior of a new composite ternary system: WO₃/SiC-TiO₂. Effect of the coupling of semiconductors and oxides in photocatalytic oxidation of methylethylketone in the gas phase," *Catalysis Communications*, vol. 4, no. 8, pp. 377–383, 2003.
- [31] V. Jokanovic, D. Janackovic, P. Spasic, and D. Uskokovic, "Modeling of nanostructural design of ultrafine mullite powder particles obtained by ultrasonic spray pyrolysis," *Nanostructured Materials*, vol. 12, no. 1, pp. 349–352, 1999.
- [32] P. G. Smetad and M. Graetzel, "Demonstrating electron transfer and nanotechnology: a natural dye-sensitized nanocrystalline energy converter," *Journal of Chemical Education*, vol. 75, no. 6, p. 752, 1999.
- [33] J. B. Gunn, "Microwave oscillations of current in III-V semiconductors," *Solid State Communications*, vol. 1, no. 4, pp. 88–91, 1963.
- [34] R. G. Cope and A. W. Penn, "High-speed solid-state thermal switches based on vanadium dioxide," *Journal of Physics D*, vol. 1, no. 2, pp. 161–168, 1968.
- [35] G. Stefanovich, A. Pergament, and D. Stefanovich, "Electrical switching and Mott transition in VO₂," *Journal of Physics Condensed Matter*, vol. 12, no. 41, pp. 8837–8845, 2000.
- [36] L. Shikwambana, M. Govender, B. Mwakikunga, E. Sideras-Haddad, and A. Forbes, "A review of the laser pyrolysis technique used to synthesize vanadium and tungsten oxide thin films," *Advanced Materials Research*, vol. 227, pp. 80–83, 2011.
- [37] B. W. Mwakikunga, A. E. Mudau, N. Brink, and C. J. Willers, "Flame temperature trends in reacting vanadium and tungsten ethoxide fluid sprays during CO₂-laser pyrolysis," *Applied Physics B*, vol. 105, pp. 451–462, 2011.
- [38] B. W. Mwakikunga M Maaza, K. T. Hillie, C. J. Arendse, T. Malwela, and E. Sideras-Haddad, "From phonon confinement to phonon splitting in flat nanostructures: a case of VO₂@V₂O₅ core-shell nanoribbons," *Vibrational Spectroscopy*, vol. 61, pp. 105–111, 2012.



Hindawi

Submit your manuscripts at
<http://www.hindawi.com>

